Pore Size Distribution Controls Dynamic Permeability

Jimmy X. Li[1], **Reza Rezaee**[1], **Tobias M. Müller**[2], **and Mohammad Sarmadivaleh** [1]

[1]Western Australian School of Mines, Curtin University, Kensington, WA 6151, Australia.
[2]Department of Seismology, Centro de Investigacion Cientifica y de Educacion Superior de Ensenada, 22860 Ensenada, BC, Mexico.

Key Points:

- We propose a dynamic permeability model revealing that the pore size distribution has a first-order effect on the dynamic permeability
- The effect of wettability on the dynamic permeability is explored by the implementation of the slip boundary condition
- The proposed model builds a connection between signatures of elastic waves and the nuclear magnetic resonance technique

Corresponding author: Jimmy X. Li, `Jimmy.Li@postgrad.curtin.edu.au`, `26 Dick Perry Avenue, Kensington, WA 6151, Australia.`

Abstract

Probing the flow permeability of porous media with elastic waves is a formidable challenge, also because the wave-induced oscillatory motion renders the permeability frequency dependent. Existing theoretical models for such a dynamic permeability assume that the frequency dependence is primarily controlled by a single characteristic length scale of the pore space. However, the fact that in most natural porous media there exists a distinct range of pore sizes is ignored. To overcome this limitation, we develop a dynamic permeability model that explicitly incorporates the pore size distribution. We show that the pore size distribution has a first-order effect on the dynamic permeability. Since the pore size distribution is measurable from techniques such as nuclear magnetic resonance, the results indicate the possibility to jointly use remote-sensing technologies for improved geomaterial characterization and optimized permeability manipulation of manufactured porous media.

Plain Language Summary

The flow rate of fluid through a porous material depends on the permeability. When the porous material is excited with elastic waves, there is oscillatory fluid motion in the pore network. Then the permeability becomes frequency-dependent, i.e. a dynamic permeability. We develop a model for the dynamic permeability in porous materials with a range of pore sizes. We find that the pore sizes and their pore volume fraction have significant influence on the dynamic permeability. This is the first time to make connection between the elastic wave, whose velocity and attenuation are controlled by the dynamic permeability, and the nuclear magnetic resonance technique from which the pore size distribution can be inferred.

1 Introduction

Analogous to the dc and ac electrical conductivity of metals, the dc and ac permeability are prime characteristics of a porous medium. The estimation of the flow (dc) permeability in presence of a fluid pressure gradient is of uttermost importance in geofluid detection (Chu et al., 1988; Blunt, 2017), water resource management and development (Molz et al., 1989; Neuzil, 1986; Ghanbarian et al., 2016), biomechanics and mechanobiology (Gailani et al., 2009; Benalla et al., 2012; Cardoso et al., 2013), nuclear waste disposal and storage (Reynes et al., 2001; Liu, 2014), and chemical engineering (Xue et al., 2018). When the fluid pressure gradient is time-harmonic, e.g. when induced by elastic waves, oscillatory motion arises and then the ac (dynamic) permeability concept originally developed by Johnson et al. (1987) is essential with direct applications in borehole acoustics (Lin et al., 2009; Zhang and Müller, 2019).

The so-called JKD model of Johnson et al. (1987) for the ac permeability is known to work well in porous media with relatively simple pore structures. Various theoretical and numerical analyses point out the limitations of the JKD model in presence of corrugated pore channels as typically observed in porous rocks. Then, the bulk fluid flow contribution dominates the flow in the viscous boundary layer (VBL), resulting in slower convergence of the dynamic permeability to its high-frequency asymptotic limit (Achdou & Avellaneda, 1992; Cortis et al., 2003). The importance of pore sizes and their distribution on the hydrodynamics of oscillating flows has also been recognized (Achdou & Avellaneda, 1992). Given that the pore sizes in rocks are highly variable and their spatial distribution is complex, one expects that the ac permeability is strongly controlled by the pore size distribution (PSD). However, its impact is typically neglected or oversimplified, e.g. by roughly estimating parameters in the existing dynamic permeability models (Müller & Sahay, 2011; Pazdniakou & Adler, 2013). This is striking since the pore size distribution in rocks is measurable in the laboratory and in-situ in boreholes.

Perhaps the most popular laboratory technique for PSD determination is mercury injection capillary pressure (MICP) experiment (Purcell et al., 1949). However, due to environmental and economic concerns, modern approaches construct the capillary pressure curve and the PSD from nuclear magnetic resonance measurements (NMR) (Eslami et al., 2013; Xiao et al., 2016). It is also common to extract the PSD from image analysis of scanning electron microscopy (SEM) or micro computed tomography (μ-CT) (Blunt, 2017; Widiatmoko et al., 2010) with excellent visualisation of pore structure. However, such image-based PSD is often restricted to very small areas or sub-volumes making it unrepresentative for macroscopic formations. Thus, from this perspective, the PSDs from NMR or MICP are better choices since they provide averaged values (i.e. core or even larger scale) and yet sufficient detail to represent macroscopic spatial variations. Especially, the inversion of PSD from NMR spectra is of great practical significance given its potential applicability in well-bore intervals. In this letter we construct a dynamic permeability model that incorporates the broadband PSD derived from NMR measurements.

2 Theory

2.1 Hydrodynamics of Oscillating Flow at Pore-scale

Let us consider a representative pore channel saturated by a viscous fluid with shear viscosity μ_f and density ρ_f. Under the action of an externally imposed, harmonic loading $\mathrm{e}^{-\mathrm{i}\omega t}$, a fluid parcel performs an oscillatory movement along the channel axis. The fluid velocity $\mathbf{u}$ can be decomposed into a potential flow field $\mathbf{u}_\mathrm{p}$ and a viscous flow field due to the drag of the pore wall (Lighthill & Lighthill, 2001; Biot, 1956b)

$$\mathbf{u} = \mathbf{u}_\mathrm{p}\left[1 - \tilde{v}\right], \tag{1}$$

where $\tilde{v}$ is conceived as the viscous flow velocity normalized by $|\mathbf{u}_\mathrm{p}|$. Only the viscous flow contributes to the Darcy flow observed at macro-scale and through which the dc permeability is defined. In contrast, the potential flow is independent of the shear viscosity. With increasing frequency, the viscous skin depth $\delta = \sqrt{2\mu_\mathrm{f}/\rho_\mathrm{f}\omega}$ becomes very small and the oscillatory flow is dominated by the flow in the bulk volume (Cortis et al., 2003). Thus, with increasing frequency the dc permeability is expected to vanish and the frequency-dependent transition is governed by the ac permeability. For idealized pore geometries, the normalized velocity of bulk flow is a function of pore size r:

$$\tilde{v}\big(k(\omega); r\big) = \begin{cases} \mathrm{e}^{\mathrm{i}kr} & \text{Flat pore wall} \\ \cosh^{-1}(\mathrm{i}kr) & \text{Slit pore} \\ \mathrm{J}_0^{-1}(kr) & \text{Cylindrical pore} \end{cases} \tag{2}$$

Here r is half of the aperture length for planar and slit-like pores or the radius for the cylindrical pore. The viscous wave describing the process of vorticity diffusion has the wave number $k = (1 + \mathrm{i})/\delta$. For an assemblage of pores, i.e. a porous medium with porosity ϕ, the dc permeability is proportional to the square of the effective hydraulic length scale r_{h}, i.e. $\kappa_0 \propto r_{\mathrm{h}}^2$. This dc permeability becomes only meaningful for a low-frequency regime $\delta \gg r_{\mathrm{h}}$, but not for a high-frequency regime when potential flow prevails as $\delta \ll r_{\mathrm{h}}$. The crossover frequency is the Biot frequency (Biot, 1956a) scaled by the tortuosity T: $\omega_B = \phi\mu_{\mathrm{f}}/T\kappa_0\rho_{\mathrm{f}}$ (Sheng & Zhou, 1988; Charlaix et al., 1988).

2.2 Interaction of Propagating and Diffusive Waves at Macro-scale

The volume averaging framework of poroelasticity systematically brings the role of the diffusive viscous wave to the macroscopic level, i.e. at scale of a porous medium containing one or multiple pore networks (Sahay et al., 2001). The diffusive viscous wave in the VBL emerges at macro-scale as slow shear (S-) wave, which is the fourth kind of wave in fluid- saturated porous media (Sahay, 2008). Such a macroscopic description has the advantage that then the interaction with elastic waves can be quantified. The conversion scattering from fast P- to slow S-waves in a weak-fluctuation approximation results in an effective P-wavenumber (Müller & Sahay, 2011)

$$k_1 \simeq k_1^{\infty} \left[1 + \Delta_1\left(1 + k_4^2\,\tilde{\ell}^2\right)\right] . \tag{3}$$

This means that an incoming P-wave (k_1^{∞}) is becoming attenuated due to conversion into the slow S-wave (k_4), or equivalently, due to the presence of VBL. Δ_1 represents a combination of variances of the randomly fluctuating medium parameters and $\tilde{\ell}^2$ contains their characteristic length scales. Similarly, a propagating slow$P$-wave k_2^{∞} is becoming attenuated due to conversion scattering into the slow S-wave according to (Müller & Sahay, 2011)

$$k_2 \simeq k_2^{\infty} \left[1 + \Delta_1\left(1 + k_4^2\,\tilde{\ell}^2\right)\right] . \tag{4}$$

In equations. (3) and (4) the complex-valued slow S-wave number is $k_4 = k_- + \mathrm{i}k_+$ with

$$k_{\mp} = \sqrt{\frac{\omega\rho_{\mathrm{f}}}{2d_{\mathrm{f}}\mu_{\mathrm{f}}}}\sqrt{\sqrt{(1 + d_{\mathrm{f}}m_{\mathrm{f}})^2 + \frac{\omega_B^2}{\omega^2}} \mp \frac{\omega_B}{\omega}}, \tag{5}$$

where $d_{\mathrm{f}} = 1/(T - m_{\mathrm{f}})$, $m_{\mathrm{f}} = \phi\rho_{\mathrm{f}}/[\phi\rho_{\mathrm{f}} + (1-\phi)\rho_s]$ is the fluid mass fraction, ρ_s is the density of the solid. Thus, in the porous medium context the normalized velocity of bulk flow $\tilde{v}(\omega; r)$ is obtained by replacing the wave number of ordinary diffusive wave k in equation (2) by the slow S-wave number k_4.

2.3 Dynamic Permeability Based on Pore Size Distribution

Müller and Sahay (2011) draw an analogy between the slow P-wave in the inertial regime (k_2^∞) and the potential flow field to develop a model for the dynamic permeability based on the frequency-dependent $k_2 \to k_4$ conversion scattering process. Key to this model is the interpretation of the dynamic length scale in equations. (3) and (4),

$$\tilde{\ell}^2 = \int_0^\infty r\, B(r)\, \mathrm{e}^{\mathrm{i}k_4 r}\, dr\,. \tag{6}$$

It arises due to the presence of random heterogeneity, whose spatial correlation function is $B(r)$, and the slow S-wave number k_4 as proxy for the vorticity diffusion process in the VBL. We remark that the use of equation (6) for heterogeneous porous media is permitted since equations (3) and (4) are macroscopic equations. Here, we conceptualize the heterogeneous porous medium as a medium in which the sub-porosity is variable in space. For such a multiple porosity medium we assign to each incremental porosity ϕ_i a characteristic hydraulic length r, which quantifies the dominant pore size associated with the spatial domain of ϕ_i. This is symbolically denoted as $\phi_i(r)$. We assume that this length is variable within a range $r \in [r_{\min}, r_{\max}]$. Then, the dynamic length scale becomes

$$\tilde{\ell}^2 = \int_{r_{\min}}^{r_{\max}} r\, \phi_i(r)\, \tilde{v}\big(k_4(\omega); r\big)\, dr\,. \tag{7}$$

We note that the finite range of integration replaces the requirement of a vanishing $B(r \to \infty)$ in the original weak-fluctuation approximation. Since laboratory measurements of the pore size and the corresponding distribution of the incremental porosity are discrete quantities, we discretizise the integral. Assuming that there are n different characteristic hydraulic lengths in $[r_{\min}, r_{\max}]$ with an increment $\Delta r = (r_{\max} - r_{\min})/n$, we find

$$\tilde{\ell}^2 = \sum_{r=r_{\min}}^{r_{\max}} r\, \phi_i(r)\, \tilde{v}\big(k_4(\omega); r\big)\, \Delta r\,. \tag{8}$$

Without the oscillating perturbation, the $\tilde{\ell}$ defined in equation (8) is a length scale $\tilde{\ell}(k_4 = 0) = \sqrt{r_a \Delta r}$ associated with the average pore size $r_\mathrm{a} = \sum r\phi_i$. The incremental porosity ϕ_i is the calibrated porosity associated with all pores of the i^{th} pore size (Coates et al., 1999). Under excitation of external harmonic loading, the frequency-dependent square of length scale $\tilde{\ell}^2$ controls the amount of the fluid in the porous medium contributing to Darcy flow. Therefore, the term $\Delta_1 \tilde{\ell}^2$ in equations (3) and (4) acts as the dynamic permeability. In the low-frequency limit, the dynamic permeability is not arbitrary but has to converge to the dc permeability. Thus, the dynamic permeability incorporating a discrete PSD (with measured r and ϕ_i) is

$$\tilde{\kappa}(\omega) = \kappa_0 \sum_{r=r_{\min}}^{r_{\max}} r\,\phi_i(r)\,\tilde{v}\big(k_4(\omega); r\big) \Big/ \sum_{r=r_{\min}}^{r_{\max}} r\,\phi_i(r)\,\tilde{v}\big(k_4^0; r\big)\,, \tag{9}$$

where $k_4^0 \equiv k_4(\omega \to 0) = \mathrm{i}\sqrt{\phi/\kappa_0 T d_{\mathrm{f}}}$. Equation (9) is the main result of this letter. It allows us to quantify the dynamic permeability in porous media with multiple porosity peaks in the discrete PSD which is measurable by using experimental techniques such as NMR. Thus, equation (9) provides a crosslink between the two entirely different experimental techniques of seismic sounding and NMR.

2.4 Dynamic Permeability for Different Wettability Conditions

Based on the different hydrodynamic behavior of fluids on hydrophobic and hydrophilic solid surfaces, the impact of the wettability on the dynamic permeability is represented by the slip boundary condition (SBC) (Li, Rezaee, & Müller, 2020; Li, Rezaee, Müller, & Sarmadivaleh, 2020). The wettability indicator, the static contact angle θ_c for the liquid cluster immersed in its vapor on a solid surface, and the slip length b follow the scaling relationship $b \propto (1+\cos\theta_c)^{-2}$ (Huang et al., 2008; Ortiz-Young et al., 2013). Thus, the wettability of a porous medium can be modeled by a variable slip length ($b \geq 0$). The effective shear viscosity corresponding to SBC is the apparent viscosity of the fluid inside the VBL (Li, Rezaee, Müller, & Sarmadivaleh, 2020),

$$\mu_{\mathrm{f}}^{\mathrm{slip}} = \frac{\mu_{\mathrm{f}}}{1 + \frac{b}{\delta_p(\omega)}}\,, \tag{10}$$

where $\delta_p(\omega) = |(1+\mathrm{i})/k_4|$ is a modified viscous skin depth. This approximation implies that the VBL has finite thickness in the low frequency limit, $\delta_p^0 = |(1+\mathrm{i})/k_4^0|$. Thus, $\mu_{\mathrm{f}}^{\mathrm{slip}}(\omega \to 0) = \frac{\mu_{\mathrm{f}}}{1+b/\delta_p^0} < \mu_{\mathrm{f}}$, which in turn implies that the effective dc permeability exceeds κ_0,

$$\kappa_0^{\mathrm{slip}} = \kappa_0 \left(1 + \frac{b}{\delta_p^0}\right) > \kappa_0\,. \tag{11}$$

This means that a hydrophobic porous medium saturated by a non-wetting fluid corresponds to the SBC where the effective dc permeability is higher than that in the case of wetting fluid saturation, in agreement with Javadpour et al. (2015). There is also a close resemblance to the model of Berg et al. (2008). By using the effective viscosity $\mu_{\mathrm{f}}^{\mathrm{slip}}$ and the effective dc permeability κ_0^{slip} for SBC in equation (9) we obtain a generalization of the dynamic permeability model to account for the wettability condition.

3 Implications in Pseudo and Real Sandstone

3.1 Dynamic Permeability for Bimodal PSD

In order to evaluate the impact of PSD on dynamic permeability, we construct two different bimodal pore size distributions often observed for rocks (Xiao et al., 2016). The PSD of example #1 includes a large portion of big pores and a only little portion of small pores, a typical feature for conventional sandstones (black curve in Figure 1a and b). In contrast, in example #2 the PSD means that pore volume of small sized pores comprise a large portion of the pore volume than that of large size pores. This is a characteristic of so-called tight rocks (red curve in Figure 1a and b). Real and imaginary parts of the dynamic permeability (without and with SBC) are shown in Figure 1c and d. To investigate the effect of PSD solely, we use in both examples the parameters given in Table 1. The slip length is arbitrarily chosen as $b = 0.1\, r_e$ for the SBC, where the effective capillary radius $r_e = 5\sqrt{\kappa_0/\phi}$ (Blunt, 2017; Berg et al., 2008).

The imaginary part of hydrophobic case is higher in low frequencies but lower in high frequencies than that of hydrophilic case indicating that the hydrophobicity of SBC promotes the relative motion of fluid, therefore increase the dissipation, in low frequencies but diminishes the viscous friction at high frequencies (Figure 1d).

In contrast to the smooth crossover predicted by the JKD model, the PSD-dependent dynamic permeability exhibits quite different patterns. This is because the variability of the pore sizes is embedded in our model. The imaginary parts have two peaks, which is especially prominent for the tight rock because of its large portion of the pore volume comprised of small size pores. The Biot frequency coincides with the low frequency peak indicating the general validity of the relation $\tilde{\kappa}(\omega)/\kappa_0 = f(\omega/\omega_B)$ with the corresponding characteristic pore size $r_c \sim \sqrt{\kappa_0/\phi}$. The high-frequency peaks arise due to the presence of a smaller characteristic pore sizes.

3.2 Dynamic Permeability for Measured PSD

We infer the pore sizes and their distribution for a Bentheimer sandstone sample by using the Magritek 2 MHz NMR Rock Core Analyzer. Following the experimental protocol of Xiao et al. (2016), we obtain 53 data points of the true pore size distribution from the NMR T_2 (transverse relaxation time) distribution data, which is subsequently calibrated by the mercury injection pore radii distribution (Figure 2a and b). The SEM

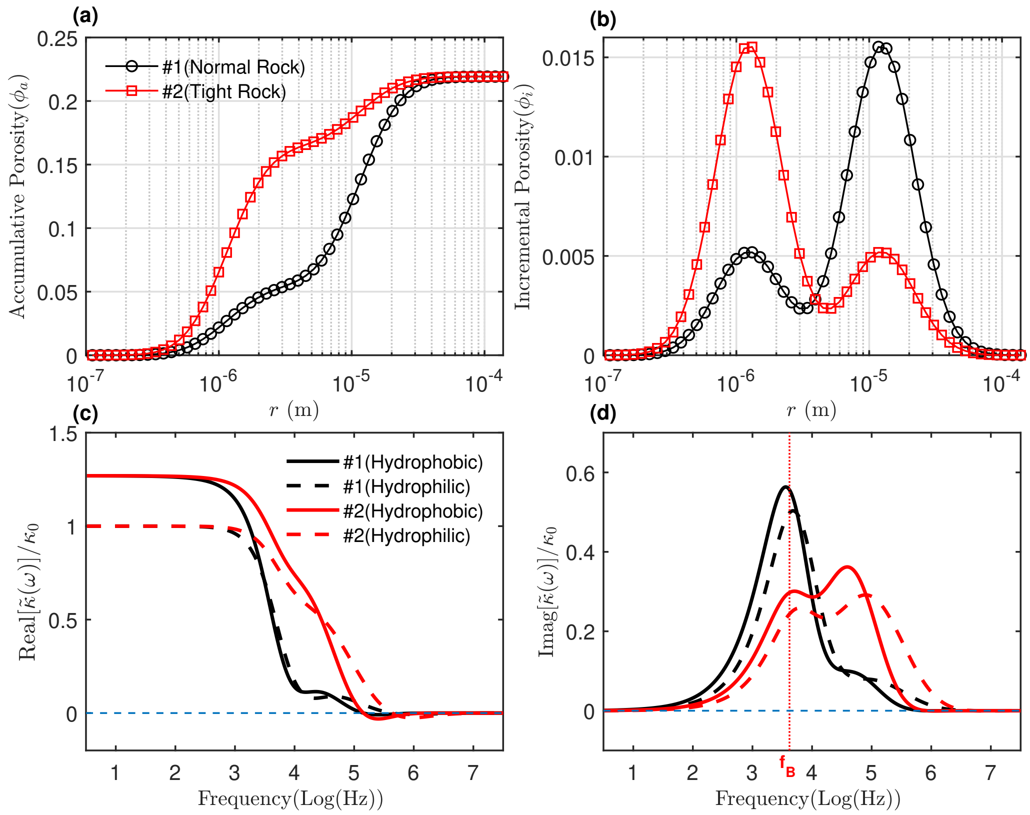

Figure 1. (**a**) Accumulative and (**b**) incremental porosity of two bimodal pore size distributions; (**c**) real and (**d**) imaginary part of the dynamic permeability and approximation in the slip boundary (hydrophobic) condition. The horizontal dash lines indicate the zero values. The vertical dotted line marks the Biot frequency $f_B = \omega_B/2\pi$.

image is taken at the same time for grain shape/sorting analysis (inset of Figure 2a), which also illustrates the complexity of pore spaces (light red shading in inset of Figure 2b).

Using the parameters in Table 1, the real parts and imaginary parts of normalized dynamic permeability are shown in Figure 2c and d. The dynamic permeability based on PSD has a lot of similarities with other dynamic permeability models (Achdou & Avellaneda, 1992; Johnson et al., 1987; Müller & Sahay, 2011; Sheng & Zhou, 1988). For instance, the scaling function $\tilde{\kappa}/\kappa_o = f(\omega/\omega_B)$ is validated for the dynamic permeability based on PSD (Figure 2). It is clearly segmented by the Biot frequency $f_B = \omega_B/2\pi$ into two parts: the viscous dominated regime in low frequencies ($f \ll f_B$) where $\tilde{\kappa} \simeq \kappa_0$ and the inertia dominated regime at high frequencies ($f \gg f_B$), where the dynamic

Table 1. Parameters of Water-saturated Bentheimer Sandstone

Grain	
Density, ρ_s	2650 kg/m^3
Matrix Frame	
Porosity, ϕ	0.2192
dc Permeability *, κ_0	$3{\times}10^{-12}$ m^2
Tortuosity **, T	2.78
Fluid	
Density, $\rho_{\rm f}$	1000 kg/m^3
Viscosity, $\mu_{\rm f}$	1 cP

* Klinkenberg Permeability.

** Estimated by $T = \frac{1}{2}(1 + 1/\phi)$ (Berryman & Thigpen, 1985).

permeability decreases as frequency increases. The featured bow-tie shape imaginary part of $\tilde{\kappa}$ is also predicted. The difference between the three pore shape models of PSD dependent dynamic permeability is insignificant, especially in the low-frequency range, thus validating the insensitivity of the dynamic permeability to the microstructure (Sheng & Zhou, 1988).

3.3 Characteristic Frequencies

In Figures 1d and 2d the Biot frequency f_B matches the main peak of the imaginary part of the dynamic permeability very well. In addition we observe that at high frequencies there are further characteristic frequencies associated with characteristic pore sizes. Because the dynamic permeability model involves the slow S-wave, a characteristic frequency f_c arises when the slow S wavelength λ is on the order of the characteristic pore size of a certain pore network. Substituting equation (5) for the slow S-wave number into $k_4 = 2\pi/\lambda$, we find

$$f_c = \frac{2\mu_{\rm f}}{T\rho_{\rm f}}\sqrt{\frac{4\pi^2}{\lambda^4} + \frac{\phi/(\kappa_0 T d_{\rm f})}{\lambda^2}}\,. \qquad (12)$$

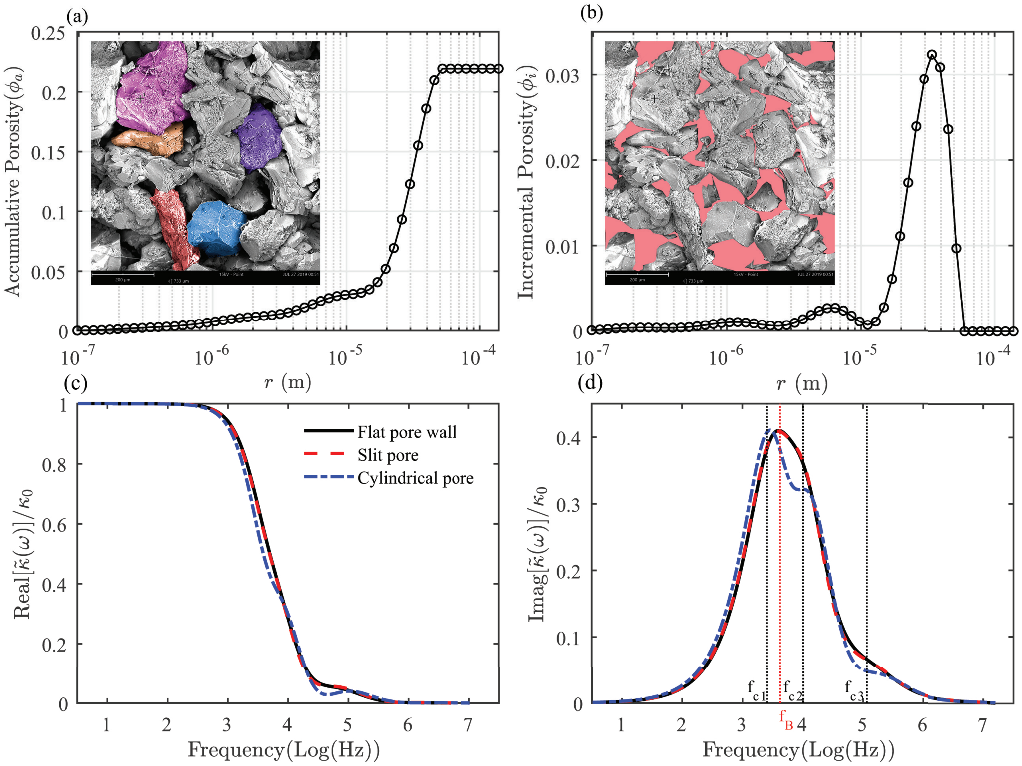

Figure 2. The pore sizes and the distribution of (**a**) accumulative and (**b**) incremental porosity for Bentheimer sandstone obtained from NMR $T2$ data (53 measurement points) calibrated by the pore throat radii distribution of MICP; SEM image in the insets demonstrates the Bentheimer sandstone has well-sorted grain framework but complicated pore network structure (light red shading in (**b**)). A comparison of the (**c**) real parts and (**d**) imaginary parts of the dynamic permeability normalized by dc permeability for the Bentheimer sandstone by three different pore shape models. The Biot frequency f_B is marked in the red dash line. The characteristic frequencies f_{c1}, f_{c2}, f_{c3} are associated with the characteristic pore sizes.

At the high frequencies, $f \gg f_B$, we have $1/\lambda^4 \gg 1/\lambda^2$ and thus

$$f_c = \frac{4\pi\mu_{\mathrm{f}}}{T\rho_{\mathrm{f}}\lambda^2}\,. \tag{13}$$

Interestingly, the characteristic pore sizes are not necessarily the pore sizes with local porosity extremes in the pore size distribution but rather they represent the local extremes of contribution to the bulk viscous flow, and hence the Darcy flow.

According to equation (8), the dynamic permeability is controlled by the frequency-dependent length scale $L_i(\omega; r) = r\phi_i\tilde{v}$. The local peaks in the imaginary part are linked

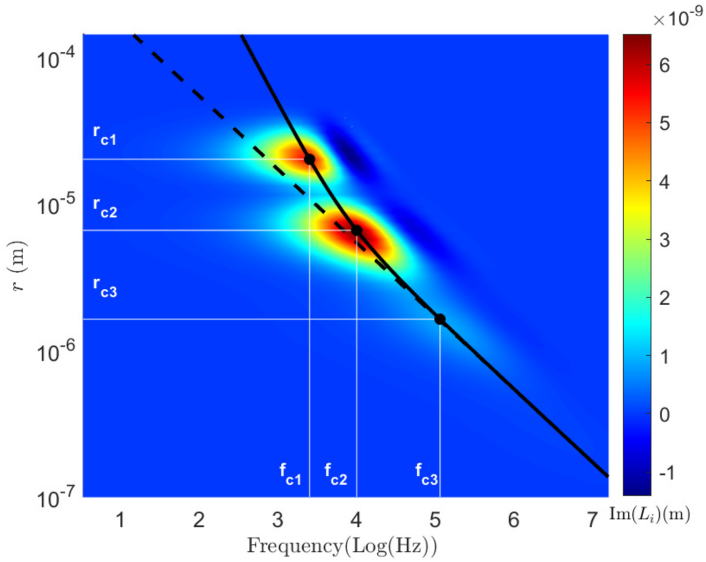

Figure 3. Imaginary part of the length scale $L_i(\omega; r) = r\phi_i\tilde{v}$ as a function of frequency and pore size where the solid black line ($\lambda \approx 4r$) based on equation (12) corresponds to the pore-scale dissipation peaks and the high-frequency linear asymptotic approximation based on equation (13) is plotted as dashed lines.

by the characteristic pore sizes (i.e. r_{c1}, r_{c2}, r_{c3} for Bentheimer sandstone) and the corresponding characteristic frequencies (Figure 3) when the slow S-wavelength approaches the characteristic pore sizes $\lambda \approx 4r_c$. These sub-characteristic frequencies (i.e. f_{c1}, f_{c2}, f_{c3} for Bentheimer sandstone) result in the piece-wise curvature pattern in the dynamic permeability (Figure 2c,d).

4 Discussion and Conclusions

We find that the dynamic permeability is controlled by the pore sizes and their distribution, but is insensitive to the microstructure, i.e. pore shapes. While this result was anticipated, our proposed model for $\tilde{\kappa}(\omega)$ makes a quantitative connection for the first time. For multimodal PSDs with distinguishable peaks additional characteristic frequencies arise, which clearly manifest in the imaginary part of the dynamic permeability as additional peaks.

The wettability condition affects not only the dynamic permeability but also the dc permeability. Interestingly, for a porous medium with parameters in Table 1, we find that the effective dc permeability in slip boundary condition (equation (11)) is equivalent to the Berg model $\kappa_0^{\text{slip}} = \kappa_0 \left(1 + C\frac{b}{r_e}\right)$ by using the constant $C \approx 3.3$. This is very close to the value ($C = 4$) obtained by Berg et al. (2008) for the end-point relative permeability of non-wetting fluid saturation.

There are broader implications. The proposed model provides a link between PSD as obtained by NMR measurements and the dynamic permeability, which, in turn, controls attenuation and dispersion of seismic waves at high frequencies, say sonic waves and ultrasound. For example, in boreholes, either Stoneley wave or NMR can be applied to estimate the formation permeability. Therefore, in principle, the proposed model might lead to cross-fertilization of experimental and in-field techniques. Moreover, since the dynamic permeability is an integral part of seismoelectric theory we expect that our model gives further impetus in analysis of seismoelectric signals. We further envisage that the PSD dependent dynamic permeability model may assist in the design of synthetic porous filter, whose performance can be manipulated by tuning the dynamic permeability via ultrasound.

Acknowledgments

We thank Dr. Zhang Xiumei for the suggestion on the numerical method and Dr. Xiao Liang for the discussion on the data acquisition of the pore size distribution. This study was supported by an Australian Government Research Training Program (RTP) Scholarship. **Data and image availability:** The pore size distribution data and the scanning electron microscopy images are available at: https://doi.org/10.5281/zenodo.3999070.

References

Achdou, Y., & Avellaneda, M. (1992). Influence of pore roughness and pore-size dispersion in estimating the permeability of a porous medium from electrical measurements. *Physics of Fluids A: Fluid Dynamics*, *4*(12), 2651–2673.

Benalla, M., Cardoso, L., & Cowin, S. (2012). Analytical basis for the determination of the lacunar–canalicular permeability of bone using cyclic loading. *Biomechanics and Modeling in Mechanobiology*, *11*(6), 767–780.

Berg, S., Cense, A., Hofman, J., & Smits, R. (2008). Two-phase flow in porous media with slip boundary condition. *Transport in Porous Media*, *74*(3), 275–292.

Berryman, J. G., & Thigpen, L. (1985). Effective constants for wave propagation through partially saturated porous media. *Applied Physics Letters*, *46*(8), 722–

724.

Biot, M. (1956a). Theory of elastic waves in a fluid-saturated porous solid. 1. low frequency range. *The Journal of the Acoustical Society of America*, *28*, 168–178.

Biot, M. (1956b). Theory of propagation of elastic waves in a fluid-saturated porous solid. ii. higher frequency range. *The Journal of the Acoustical Society of America*, *28*(2), 179–191.

Blunt, M. J. (2017). *Multiphase flow in permeable media: A pore-scale perspective.* Cambridge University Press.

Cardoso, L., Fritton, S. P., Gailani, G., Benalla, M., & Cowin, S. C. (2013). Advances in assessment of bone porosity, permeability and interstitial fluid flow. *Journal of Biomechanics*, *46*(2), 253–265.

Charlaix, E., Kushnick, A., & Stokes, J. (1988). Experimental study of dynamic permeability in porous media. *Physical Review Letters*, *61*(14), 1595.

Chu, A., Chung, H. S., Hoskin, D. H., Mitchell, T. O., & Shu, P. (1988, October 11). *Oil reservoir permeability control.* Google Patents. (US Patent 4,776,398)

Coates, G. R., Xiao, L., Prammer, M. G., et al. (1999). *NMR logging: principles and applications* (Vol. 234). Haliburton Energy Services Houston.

Cortis, A., Smeulders, D. M., Guermond, J. L., & Lafarge, D. (2003). Influence of pore roughness on high-frequency permeability. *Physics of Fluids*, *15*(6), 1766–1775.

Eslami, M., Kadkhodaie-Ilkhchi, A., Sharghi, Y., & Golsanami, N. (2013). Construction of synthetic capillary pressure curves from the joint use of nmr log data and conventional well logs. *Journal of Petroleum Science and Engineering*, *111*, 50–58.

Gailani, G., Benalla, M., Mahamud, R., Cowin, S. C., & Cardoso, L. (2009). Experimental determination of the permeability in the lacunar-canalicular porosity of bone. *Journal of Biomechanical Engineering*, *131*(10).

Ghanbarian, B., Sahimi, M., & Daigle, H. (2016). Modeling relative permeability of water in soil: Application of effective-medium approximation and percolation theory. *Water Resources Research*, *52*(7), 5025–5040.

Huang, D. M., Sendner, C., Horinek, D., Netz, R. R., & Bocquet, L. (2008). Water slippage versus contact angle: A quasiuniversal relationship. *Physical Review*

Letters, *101* (22), 226101.

Javadpour, F., McClure, M., & Naraghi, M. (2015). Slip-corrected liquid permeability and its effect on hydraulic fracturing and fluid loss in shale. *Fuel*, *160*, 549–559.

Johnson, D. L., Koplik, J., & Dashen, R. (1987). Theory of dynamic permeability and tortuosity in fluid-saturated porous media. *Journal of Fluid Mechanics*, *176*, 379–402.

Li, J. X., Rezaee, R., & Müller, T. M. (2020). Wettability effect on wave propagation in saturated porous medium. *The Journal of the Acoustical Society of America*, *147* (2), 911–920.

Li, J. X., Rezaee, R., Müller, T. M., & Sarmadivaleh, M. (2020). Elastic waves in porous media saturated with non-wetting fluid. *The APPEA Journal*, *60* (1), 315–325.

Lighthill, M. J., & Lighthill, J. (2001). *Waves in fluids*. Cambridge university press.

Liu, H.-H. (2014). Non-darcian flow in low-permeability media: key issues related to geological disposal of high-level nuclear waste in shale formations. *Hydrogeology Journal*, *22* (7), 1525–1534.

Molz, F. J., Morin, R. H., Hess, A. E., Melville, J. G., & Güven, O. (1989). The impeller meter for measuring aquifer permeability variations: evaluation and comparison with other tests. *Water Resources Research*, *25* (7), 1677–1683.

Müller, T. M., & Sahay, P. N. (2011). Stochastic theory of dynamic permeability in poroelastic media. *Physical Review E*, *84* (2), 026329.

Neuzil, C. E. (1986). Groundwater flow in low-permeability environments. *Water Resources Research*, *22* (8), 1163–1195.

Ortiz-Young, D., Chiu, H.-C., Kim, S., Voïtchovsky, K., & Riedo, E. (2013). The interplay between apparent viscosity and wettability in nanoconfined water. *Nature Communications*, *4* (1), 1–6.

Pazdniakou, A., & Adler, P. (2013). Dynamic permeability of porous media by the lattice boltzmann method. *Advances in Water Resources*, *62*, 292–302.

Purcell, W., et al. (1949). Capillary pressures-their measurement using mercury and the calculation of permeability therefrom. *Journal of Petroleum Technology*, *1* (02), 39–48.

Reynes, J., Woignier, T., & Phalippou, J. (2001). Permeability measurement in composite aerogels: application to nuclear waste storage. *Journal of Non-crystalline Solids*, *285*(1-3), 323–327.

Sahay, P. N. (2008). On the Biot slow S-wave. *Geophysics*, *73*(4), N19–N33.

Sahay, P. N., Spanos, T. T., & De La Cruz, V. (2001). Seismic wave propagation in inhomogeneous and anisotropic porous media. *Geophysical Journal International*, *145*(1), 209–222.

Sheng, P., & Zhou, M.-Y. (1988). Dynamic permeability in porous media. *Physical Review Letters*, *61*(14), 1591.

Widiatmoko, E., Abdullah, M., & Khairurrijal. (2010). A method to measure pore size distribution of porous materials using scanning electron microscopy images. In *Aip conference proceedings* (Vol. 1284, pp. 23–26).

Xiao, L., Mao, Z.-q., Zou, C.-c., Jin, Y., & Zhu, J.-c. (2016). A new methodology of constructing pseudo capillary pressure (pc) curves from nuclear magnetic resonance (nmr) logs. *Journal of Petroleum Science and Engineering*, *147*, 154–167.

Xue, J., Wang, S., Han, X., Wang, Y., Hua, X., & Li, J. (2018). Chitosan-functionalized graphene oxide for enhanced permeability and antifouling of ultrafiltration membranes. *Chemical Engineering & Technology*, *41*(2), 270–277.